Three-Dimensional Finite, Boundary, and Hybrid Element Solutions of the Maxwell Equations for Lossy Dielectric Media

KEITH D. PAULSEN, MEMBER, IEEE, DANIEL R. LYNCH, AND JOHN W. STROHBEHN, SENIOR MEMBER, IEEE

Abstract—**Finite, boundary, and hybrid element approaches are presented as numerical methods for computing electromagnetic (EM) fields inside lossy dielectric objects. These techniques are implemented as computer algorithms for solving the Maxwell equations in heterogeneous media in three dimensions. Algorithm verification takes the form of comparisons of test cases with analytic solutions. Computed results for each technique are in good agreement with exact solutions, especially in the light of the coarse computational grid resolutions used. Implementation was in Fortran on a moderate-sized computer (MicroVax II). The basic problem formulation is quite general; however, it has direct application in hyperthermia as a cancer therapy where the EM fields produced inside the patient by external sources are of interest. An example of the application of these numerical methods in a three-dimensional clinical setting is shown.**

I. Introduction

INTEREST IN USING numerical analysis to extract a more complete understanding of the capabilities of electromagnetic (EM) devices for producing hyperthermia in cancer patients has increased dramatically within the last several years [1], [2]. Such analyses can be performed via numerical simulations of hyperthermia cancer treatments. The simulation process can be considered a two-step procedure: (1) compute the energy deposition produced by the heat source and (2) compute the thermal redistribution due to heat conduction and blood perfusion. While the later is generic to all heat delivery systems, the first procedure is dependent on the specific source under consideration. Due to the widespread use of the EM field as such a heat source (e.g. see [3]–[5]), numerical solution of the Maxwell equations in tissue (a lossy, heterogeneous medium) is of particular interest to hyperthermia researchers. While our motivation is due to interest in the hyperthermia problem, the approaches described herein are quite general and applicable to other problems involving heterogeneous lossy dielectric objects.

Currently, we are developing numerical methods for calculating electromagnetic fields induced in the body by various EM source arrangements [6]–[10]. Several clinical devices have been modeled as boundary value problems, in which case the finite element method (FEM) with simple linear and bilinear elements has been employed to solve the Maxwell equations [6], [8], [10]. The details of the patient interior have been preserved by generating finite element grids from CT scans of actual cancer patients. A number of clinical settings, however, result in electromagnetic problems which are fundamentally unbounded. For these situations a hybrid element method (HEM) has been devised where finite elements, which are used inside the heterogeneous patient, are coupled to boundary elements, which are used on the patient surface and detached EM source [7]. Thus far, all of our results have been restricted to two dimensions, where both the transverse magnetic and transverse electric cases have been studied. Other numerical approaches to solving the Maxwell equations in the context of two-dimensional hyperthermia treatment simulation have been reported, and examples of such are [11]–[13].

While these two-dimensional computed results have been informative and agree with limited available data, there exists a need for detailed three-dimensional solutions of the Maxwell equations in hyperthermia treatment simulations. Since the cross-sectional dimensions of many treatment situations are on the order of the longitudinal dimension, the propriety of making two-dimensional assumptions remains an open question. Full three-dimensional solutions are a required component in establishing the degree of validity of such two-dimensional assumptions. Further, some phenomena, such as resonances in the body extremities or effects of longitudinal tissue variations, which may play an important role in understanding the capabilities of certain EM therapy devices, cannot be readily studied with two-dimensional models, but must be addressed with three-dimensional simulations. Finally, since the physical problem of interest is truly three-dimensional due to the

Manuscript received May 4, 1987; revised October 22, 1987. This work was supported in part by the DHHS/NIH/NCI under Grants CA-37245 and CA-45357 and by the NSF under Grant CEE-8352226.

K. D. Paulsen is with the Department of Electrical and Computer Engineering, University of Arizona, Tucson, AZ 85721.

D. R. Lynch and J. W. Strohbehn are with the Thayer School of Engineering, Dartmouth College, Hanover, NH 03755.

IEEE Log Number 8719205.

0018-9480/88/0400-0682$01.00 ©1988 IEEE

vector nature of the EM field and the arbitrary tissue variation in all directions, the most realistic and accurate simulations will result from three-dimensional models.

Three-dimensional solutions of EM fields induced in biological tissue have been reported in the literature. A scattering formulation resulting in domain integral equations which were solved via the method of moments has been implemented and the details of the approach can be found in [14]. A number of researchers have used this approach to calculate EM fields induced in three-dimensional block models of man in the context of potential health hazards due to EM radiation (e.g. see [14], [15]). More recently, this same formulation has been used to analyze the heating of tissue placed between parallel capacitive plates [16] and to study the power deposition inside the body but outside the area of direct exposure [17]. While such studies were based on fully three-dimensional calculations which were pioneering in nature, the models of man that were used were intended to study gross effects rather than detailed energy deposition patterns. In order to increase the computational resolution to that necessary for making detailed EM field calculations inside the body, most investigators, to date, have been forced to make simplifying assumptions to reduce the problem to a two-dimensional calculation. Studies based on the finite-difference time-domain method are beginning to emerge where detailed three-dimensional energy deposition patterns are being calculated inside the body [18], [19].

In previous papers [6], [7] we have presented finite, boundary, and hybrid element numerical methods for computing detailed EM fields in the body as three-dimensional formulations, but have only numerically implemented and verified their two-dimensional counterparts. In this paper, we present the three-dimensional numerical implementations and verifications of these approaches. We begin with a discussion of our finite, boundary, and hybrid element formulations as a review and consolidation of these approaches, which heretofore have been presented independently. Some additional details of the three-dimensional implementations of boundary conditions and the hybrid coupling are also provided. The verification of the three-dimensional algorithms takes the form of comparisons with known analytic solutions. Our purpose here is not to provide a study which focuses on comparing the algebraic requirements and accuracy of these three methods, but rather to illustrate that our numerical formulations can be implemented in three dimensions with good accuracy, yet without any unusual complications or unforeseen problems. Finally, an example which is relevant to clinical hyperthermia is shown. This work should provide a foundation upon which detailed three-dimensional calculations of EM fields induced in the body can be made.

II. Mathematical Formulation

The second-order partial differential equations in the quantities of interest—either $\boldsymbol{E}$ or $\boldsymbol{H}$—which need to be solved are

$$\nabla \times \frac{1}{i\omega\mu} \nabla \times \boldsymbol{E} + i\omega\epsilon^* \boldsymbol{E} = 0 \tag{1a}$$

$$\nabla \times \frac{1}{i\omega\epsilon^*} \nabla \times \boldsymbol{H} + i\omega\mu \boldsymbol{H} = 0 \tag{1b}$$

where

- $\boldsymbol{E}$ complex amplitude of the electric field,
- $\boldsymbol{H}$ complex amplitude of the magnetic field,
- μ magnetic permeability,
- $\epsilon^* = \epsilon + i\sigma/\omega$, complex permittivity,
- ϵ permittivity,
- σ electrical conductivity,
- ω radian frequency,
- $i = \sqrt{-1}$.

In addition, a periodic time variation of the form $e^{-i\omega t}$ has been assumed. Since (1a) and (1b) are to be enforced in a heterogeneous medium, certain boundary conditions must be imposed on $\boldsymbol{E}$ and $\boldsymbol{H}$ at interfaces where the electrical properties change abruptly. Assuming no electromagnetic sources are present, these conditions can be stated as

$$\hat{\boldsymbol{n}} \cdot (\epsilon_1^* \boldsymbol{E}_1 - \epsilon_2^* \boldsymbol{E}_2) = 0 \tag{2a}$$

$$\hat{\boldsymbol{n}} \times (\boldsymbol{E}_1 - \boldsymbol{E}_2) = 0 \tag{2b}$$

$$\hat{\boldsymbol{n}} \times (\boldsymbol{H}_1 - \boldsymbol{H}_2) = 0 \tag{2c}$$

$$\hat{\boldsymbol{n}} \cdot (\mu_1 \boldsymbol{H}_1 - \mu_2 \boldsymbol{H}_2) = 0. \tag{2d}$$

By expressing (2a) and (2b) in a Cartesian coordinate system, $\boldsymbol{E}$ on one side of an interface can be conveniently expressed in terms of its components on the other side such that

$$\begin{Bmatrix} E_{x_2} \\ E_{y_2} \\ E_{z_2} \end{Bmatrix} = \begin{bmatrix} n_x^2 \frac{\epsilon_1^*}{\epsilon_2^*} + n_y^2 + n_z^2 & n_x n_y \left(\frac{\epsilon_1^*}{\epsilon_2^*} - 1 \right) & n_x n_z \left(\frac{\epsilon_1^*}{\epsilon_2^*} - 1 \right) \\ n_x n_y \left(\frac{\epsilon_1^*}{\epsilon_2^*} - 1 \right) & n_x^2 + n_y^2 \frac{\epsilon_1^*}{\epsilon_2^*} + n_z^2 & n_y n_z \left(\frac{\epsilon_1^*}{\epsilon_2^*} - 1 \right) \\ n_x n_z \left(\frac{\epsilon_1^*}{\epsilon_2^*} - 1 \right) & n_y n_z \left(\frac{\epsilon_1^*}{\epsilon_2^*} - 1 \right) & n_x^2 + n_y^2 + n_z^2 \frac{\epsilon_1^*}{\epsilon_2^*} \end{bmatrix} \begin{Bmatrix} E_{x_1} \\ E_{y_1} \\ E_{z_1} \end{Bmatrix} \tag{3}$$

where the subscripts distinguish the two regions forming the interface and the unit normal to the interface is $\hat{\boldsymbol{n}} = (n_x, n_y, n_z)$. A similar expression can be written for $\boldsymbol{H}$ with μ taking the place of ϵ^* in (3). Matrix equation (3) (or its equivalent for the magnetic field case) is useful for

implementing the interface boundary conditions regardless of whether the finite, boundary, or hybrid element method is used. In the context of EM-induced hyperthermia, μ is effectively constant; hence, $\boldsymbol{H}$ is continuous across interfaces. However, since σ and ϵ vary with tissue type and frequency, $\boldsymbol{E}$ is discontinuous at such boundaries.

A. Finite Element Formulation

The finite element solution is based on the weighted residual or "weak" form of (1a) and (1b) [6]:

$$\left\langle \left(\nabla \times \frac{1}{i\omega\mu} \nabla \times \boldsymbol{E} \right) \phi_i \right\rangle + \langle i\omega\epsilon^* \boldsymbol{E} \phi_i \rangle = 0 \qquad (4a)$$

$$\left\langle \left(\nabla \times \frac{1}{i\omega\epsilon^*} \nabla \times \boldsymbol{H} \right) \phi_i \right\rangle + \langle i\omega\mu \boldsymbol{H} \phi_i \rangle = 0 \qquad (4b)$$

where $\langle\ \rangle$ indicates integration over the volume and ϕ_i are any set of real scalar weighting functions. In this work ϕ_i are simple piecewise-linear or bilinear functions. An integral theorem can be used on the first term in (4a) and (4b), producing

$$\left\langle \left(\frac{1}{i\omega\mu} \nabla \times \boldsymbol{E} \right) \times \nabla \phi_i \right\rangle + \langle i\omega\epsilon^* \boldsymbol{E} \phi_i \rangle = - \oint \hat{\boldsymbol{n}} \times \boldsymbol{H} \phi_i \, ds \qquad (5a)$$

$$\left\langle \left(\frac{1}{i\omega\epsilon^*} \nabla \times \boldsymbol{H} \right) \times \nabla \phi_i \right\rangle + \langle i\omega\mu \boldsymbol{H} \phi_i \rangle = \oint \hat{\boldsymbol{n}} \times \boldsymbol{E} \phi_i \, ds \qquad (5b)$$

where $\hat{\boldsymbol{n}}$ is the outward-pointing unit normal to the surface containing the volume. The motivation for performing this operation is to expose $\hat{\boldsymbol{n}} \times \boldsymbol{H}$ as the natural boundary condition for $\boldsymbol{E}$ and, in the dual problem, to expose $\hat{\boldsymbol{n}} \times \boldsymbol{E}$ as the natural boundary condition for $\boldsymbol{H}$.

In this work a Galerkin form of (5a) is used where $\boldsymbol{E}$ and $\hat{\boldsymbol{n}} \times \boldsymbol{H}$ are expanded in terms of the weighting functions ϕ_j such that

$$\boldsymbol{E} = \sum_{j=1}^{N} \boldsymbol{E}_j \phi_j(\boldsymbol{x}) \qquad (6a)$$

$$\boldsymbol{n} \times \boldsymbol{H} = \sum_{j=1}^{N} (\hat{\boldsymbol{n}} \times \boldsymbol{H})_j \phi_j(\boldsymbol{x}) = \sum_{j=1}^{N} \boldsymbol{F}_j \phi_j(\boldsymbol{x}) \qquad (6b)$$

where $\boldsymbol{F}_j$ is introduced for notational brevity. Similarly, $\boldsymbol{H}$ and $\hat{\boldsymbol{n}} \times \boldsymbol{E}$ can be expanded with ϕ_j for a Galerkin solution of (5b). Hence, the numerical discretization is completed with the enforcement of (5) for $i = 1$ through N (where N is the total number of nodes in the discretization). Substitution of (6a) and (6b) into (5a) results in the matrix formulation

$$[A]\{\mathscr{E}\} = [B]\{\mathscr{F}\} \qquad (7)$$

where A, $\mathscr{E}$, B, and $\mathscr{F}$ comprise the complex submatrices

$$A_{ij} = \begin{pmatrix} \left\langle \frac{1}{i\omega\mu} \left(\frac{\partial\phi_j}{\partial y}\frac{\partial\phi_i}{\partial y} + \frac{\partial\phi_j}{\partial z}\frac{\partial\phi_i}{\partial z} \right) + i\omega\epsilon^*\phi_j\phi_i \right\rangle & \left\langle -\frac{1}{i\omega\mu}\frac{\partial\phi_j}{\partial x}\frac{\partial\phi_i}{\partial y} \right\rangle & \left\langle -\frac{1}{i\omega\mu}\frac{\partial\phi_j}{\partial x}\frac{\partial\phi_i}{\partial z} \right\rangle \\ \left\langle -\frac{1}{i\omega\mu}\frac{\partial\phi_j}{\partial y}\frac{\partial\phi_i}{\partial x} \right\rangle & \left\langle \frac{1}{i\omega\mu} \left(\frac{\partial\phi_j}{\partial x}\frac{\partial\phi_i}{\partial x} + \frac{\partial\phi_j}{\partial z}\frac{\partial\phi_i}{\partial z} \right) + i\omega\epsilon^*\phi_j\phi_i \right\rangle & \left\langle -\frac{1}{i\omega\mu}\frac{\partial\phi_j}{\partial y}\frac{\partial\phi_i}{\partial z} \right\rangle \\ \left\langle -\frac{1}{i\omega\mu}\frac{\partial\phi_j}{\partial z}\frac{\partial\phi_i}{\partial x} \right\rangle & \left\langle -\frac{1}{i\omega\mu}\frac{\partial\phi_j}{\partial z}\frac{\partial\phi_i}{\partial y} \right\rangle & \left\langle \frac{1}{i\omega\mu} \left(\frac{\partial\phi_j}{\partial x}\frac{\partial\phi_i}{\partial x} + \frac{\partial\phi_j}{\partial y}\frac{\partial\phi_i}{\partial y} \right) + i\omega\epsilon^*\phi_j\phi_i \right\rangle \end{pmatrix}$$

$$\mathscr{E}_j = \begin{pmatrix} E_{x_j} \\ E_{y_j} \\ E_{z_j} \end{pmatrix} \qquad B_{ij} = \begin{pmatrix} -\oint \phi_i\phi_j \, da & 0 & 0 \\ 0 & -\oint \phi_i\phi_j \, da & 0 \\ 0 & 0 & -\oint \phi_i\phi_j \, da \end{pmatrix} \qquad \mathscr{F}_j = \begin{pmatrix} F_{x_j} \\ F_{y_j} \\ F_{z_j} \end{pmatrix}$$

with i and j running from 1 to N. The dual matrix formulation for the magnetic field requires the corresponding substitutions into (5b).

The interface boundary conditions, (2a) and (2b), need to be accounted for during the assembly of matrix equation (7). Conceptually, a cut in the finite element grid is made along an interface between two tissues, but the Galerkin equation (5a) for a node located on such an interface still contains integrations over elements on each side of the boundary. The expression for $\boldsymbol{E}$, i.e. (6a), however, requires separate values of $\boldsymbol{E}_j$ on either side of the interface. Equation (3) provides the relationship between these two unknowns which is necessary to close the algebraic system.

In practice, only a single node is used to represent a point on a tissue interface. Prior to matrix assembly one of the unknowns at the interface is selected to be retained in the algebraic system, say the tissue 1 unknowns. Matrix assembly over elements in tissue 1 proceeds directly since these unknowns are part of the matrix algebra. However, during assembly of elements in tissue 2, the unknowns on this side of the interface are not represented in the column vector of unknowns to be determined, but their contributions to the matrix can be included by expressing them in terms of the tissue 1 unknowns via (3) (for the electric field case).

The application of (3) during the matrix assembly procedure proceeds in a straightforward manner provided a suitable nodal normal can be computed. The nodal normal of Gray [20] and Engleman *et al.* [21], which is based on conservation principles, is used. In three dimensions the nodal normal, $\hat{\boldsymbol{n}}_i = (n_x, n_y, n_z)$, can be computed on finite

elements as

$$n_x = \frac{1}{n}\left\langle \frac{\partial \phi_i}{\partial x} \right\rangle \qquad n_y = \frac{1}{n}\left\langle \frac{\partial \phi_i}{\partial y} \right\rangle \qquad n_z = \frac{1}{n}\left\langle \frac{\partial \phi_i}{\partial z} \right\rangle \tag{8}$$

where

$$n = \left[\left\langle \frac{\partial \phi_i}{\partial x} \right\rangle^2 + \left\langle \frac{\partial \phi_i}{\partial y} \right\rangle^2 + \left\langle \frac{\partial \phi_i}{\partial z} \right\rangle^2 \right]^{1/2}$$

and $\langle\ \rangle$ indicates domain integration only over the tissue region for which the normal is being computed.

B. Boundary Element Formulation

The boundary element method used herein is based on the vector equivalent of Green's second identity, which can be stated as

$$\int_V (\boldsymbol{Q}\cdot\nabla\times\nabla\times\boldsymbol{P} - \boldsymbol{P}\cdot\nabla\times\nabla\times\boldsymbol{Q})\, dV = \oint_S (\boldsymbol{P}\times\nabla\times\boldsymbol{Q} - \boldsymbol{Q}\times\nabla\times\boldsymbol{P})\cdot\hat{\boldsymbol{n}}\, da \tag{9}$$

where $\boldsymbol{P}$ and $\boldsymbol{Q}$ are vector functions with continuous first and second derivatives throughout V and on S [22]. To derive the boundary element expression for the electric field, let $\boldsymbol{P} = \boldsymbol{E}$ and $\boldsymbol{Q} = G\hat{\boldsymbol{a}}$, where $\hat{\boldsymbol{a}}$ is an arbitrary unit vector and G is the unbounded-space Green function satisfying the Helmholtz equation with singularity at $\boldsymbol{x} = \boldsymbol{x}'$:

$$\nabla^2 G + k^2 G = -\delta(\boldsymbol{x} - \boldsymbol{x}'). \tag{10}$$

In (10), k is the wavenumber of the unbounded space, which in general is given by $k^2 = \omega^2\mu\epsilon^*$. After some vector manipulations, it can be shown that

$$\int_V (-\nabla\cdot[(\hat{\boldsymbol{a}}\cdot\nabla G)\boldsymbol{E}] + \hat{\boldsymbol{a}}\cdot[\nabla G(\nabla\cdot\boldsymbol{E}) - \delta(\boldsymbol{x}-\boldsymbol{x}')\boldsymbol{E}])\, dV = \oint_S \hat{\boldsymbol{a}}\cdot[\nabla G\times(\boldsymbol{E}\times\hat{\boldsymbol{n}}) - i\omega\mu(\boldsymbol{H}\times\hat{\boldsymbol{n}})G]\, da \tag{11}$$

which becomes

$$\int_V \hat{\boldsymbol{a}}\cdot\{\delta(\boldsymbol{x}-\boldsymbol{x}')\boldsymbol{E}\}\, dV = -\oint_S \hat{\boldsymbol{a}}\cdot\{(\hat{\boldsymbol{n}}\times\boldsymbol{E})\times\nabla G + i\omega\mu(\hat{\boldsymbol{n}}\times\boldsymbol{H})G + (\hat{\boldsymbol{n}}\cdot\boldsymbol{E})\nabla G\}\, da \tag{12}$$

by applying the divergence theorem to the first term on the left side of (11), and assuming that V is a homogeneous source-free region with $\boldsymbol{x}'$ on S. Since $\hat{\boldsymbol{a}}$ is arbitrary, and a factor common to all terms, it follows that the boundary expression for node i located at $\boldsymbol{x}'$ on S is

$$\alpha_i \boldsymbol{E}_i = -\oint_S \{i\omega\mu(\hat{\boldsymbol{n}}\times\boldsymbol{H})G_i + (\hat{\boldsymbol{n}}\times\boldsymbol{E})\times\nabla G_i + (\hat{\boldsymbol{n}}\cdot\boldsymbol{E})\nabla G_i\}\, da \tag{13a}$$

where $\alpha_i = \int_V \delta(\boldsymbol{x}-\boldsymbol{x}_i)\, dV$ and G_i has its singularity at node i. The dual expression for the magnetic field can be derived using the same approach and can be shown to be

$$\alpha_i \boldsymbol{H}_i = \oint_S \{i\omega\epsilon^*(\hat{\boldsymbol{n}}\times\boldsymbol{E})G_i - (\hat{\boldsymbol{n}}\times\boldsymbol{H})\times\nabla G_i - (\hat{\boldsymbol{n}}\cdot\boldsymbol{H})\nabla G_i\}\, da. \tag{13b}$$

Relative to the variety of integral forms of the Maxwell equations that are available, (13a) and (13b) are computationally attractive in that only a scalar Green function is involved, the variables in the integrands are in terms of the natural boundary conditions for the electric and magnetic fields, only boundary integration is required, and sources are represented through equivalent surface fields.

As in the finite element formulation, the field variables are expressed in terms of the expansions given in (6a) and (6b) with the understanding that ϕ is only active on the boundary. With the variables discretized, N versions of (13) (where N is the number of boundary nodes) are enforced using the set of Green functions such that the ith Green function is singular at the ith node. This process carried out on (13a) results in the matrix equation

$$[C]\{\mathscr{F}\} = [D]\{\mathscr{E}\} \tag{14}$$

where D, $\mathscr{E}$, C, and $\mathscr{F}$ form the complex submatrices:

$$D_{ij} = \begin{pmatrix} \alpha_i\delta_{ij} + \oint\left(n_x\frac{\partial \mathscr{G}}{\partial x} + n_y\frac{\partial \mathscr{G}}{\partial y} + n_z\frac{\partial \mathscr{G}}{\partial z}\right)\phi_j\, da & \oint\left(n_y\frac{\partial \mathscr{G}}{\partial x} - n_x\frac{\partial \mathscr{G}}{\partial y}\right)\phi_j\, da & \oint\left(n_z\frac{\partial \mathscr{G}}{\partial x} - n_x\frac{\partial \mathscr{G}}{\partial z}\right)\phi_j\, da \\ \oint\left(n_x\frac{\partial \mathscr{G}}{\partial y} - n_y\frac{\partial \mathscr{G}}{\partial x}\right)\phi_j\, da & \alpha_i\delta_{ij} + \oint\left(n_x\frac{\partial \mathscr{G}}{\partial x} + n_y\frac{\partial \mathscr{G}}{\partial y} + n_z\frac{\partial \mathscr{G}}{\partial z}\right)\phi_j\, da & \oint\left(n_z\frac{\partial \mathscr{G}}{\partial y} - n_y\frac{\partial \mathscr{G}}{\partial z}\right)\phi_j\, da \\ \oint\left(n_x\frac{\partial \mathscr{G}}{\partial z} - n_z\frac{\partial \mathscr{G}}{\partial x}\right)\phi_j\, da & \oint\left(n_y\frac{\partial \mathscr{G}}{\partial z} - n_z\frac{\partial \mathscr{G}}{\partial y}\right)\phi_j\, da & \alpha_i\delta_{ij} + \oint\left(n_x\frac{\partial \mathscr{G}}{\partial x} + n_y\frac{\partial \mathscr{G}}{\partial y} + n_z\frac{\partial \mathscr{G}}{\partial z}\right)\phi_j\, da \end{pmatrix}$$

$$\mathscr{E}_j = \begin{Bmatrix} E_{x_j} \\ E_{y_j} \\ E_{z_j} \end{Bmatrix} \qquad C_{ij} = -\begin{pmatrix} \oint \mathscr{G}\phi_j\, da & 0 & 0 \\ 0 & \oint \mathscr{G}\phi_j\, da & 0 \\ 0 & 0 & \oint \mathscr{G}\phi_j\, da \end{pmatrix} \qquad \mathscr{F}_j = i\omega\mu\begin{Bmatrix} F_{x_j} \\ F_{y_j} \\ F_{z_j} \end{Bmatrix}$$

with $\mathcal{G} = G(\boldsymbol{x} - \boldsymbol{x}_i)$, the unit normal vector $\hat{\boldsymbol{n}} = (n_x, n_y, n_z)$, F defined by (6b), δ equal to the Kronecker delta, and i and j running from 1 to N. The dual matrix formulation for $\boldsymbol{H}$ is reached using the same procedure with (13b) as the starting point.

Matrix equation (14) provides a mechanism for calculating $\boldsymbol{E}$ on some boundary given that $\hat{\boldsymbol{n}} \times \boldsymbol{H}$ is known on that boundary or, conversely, for calculating $\hat{\boldsymbol{n}} \times \boldsymbol{H}$ given $\boldsymbol{E}$. Once both $\hat{\boldsymbol{n}} \times \boldsymbol{H}$ and $\boldsymbol{E}$ are known over some boundary, then $\boldsymbol{E}$ can be calculated in the homogeneous region either inside or outside this boundary via 13a (13b) with α equal to unity. A similar statement can be made about the dual matrix formulation involving field variables $\boldsymbol{H}$ and $\boldsymbol{n} \times \boldsymbol{E}$.

The interface conditions for multiple region domains are accounted for during the assembly of (13a) and (13b) with the same strategy outlined above for the finite element approach where the unknowns on one side of the interface are eliminated as they arise in the matrix algebra by their counterparts on the other side of the interface via (3). These conditions, as well as (13a) and (13b) themselves, require the definition of a nodal normal. In three dimensions, a nodal normal based on surface elements can be written as $\hat{\boldsymbol{n}}_i = (n_{x_i}, n_{y_i}, n_{z_i})$ where

$$n_{x_i} = \frac{1}{n}\oint_S n_x \phi_i \, da \qquad n_{y_i} = \frac{1}{n}\oint_S n_y \phi_i \, da$$

$$n_{z_i} = \frac{1}{n}\oint_S n_z \phi_i \, da \tag{15}$$

and

$$n = \left[\left(\oint_S n_x \phi_i \, da\right)^2 + \left(\oint_S n_y \phi_i \, da\right)^2 + \left(\oint_S n_z \phi_i \, da\right)^2\right]^{1/2}.$$

This is actually the definition of the nodal normal posed by Gray [20], and the expression in (8) was derived from (15) via the divergence theorem.

C. Hybrid Element Formulation

The hybrid element method [7] employs the finite element method in regions of heterogeneity and the boundary element method in regions of unbounded homogeneity. Recall that solution of the Galerkin weighted residual statement for $\boldsymbol{E}$ (eq. (5a)) via finite elements requires knowledge of $\hat{\boldsymbol{n}} \times \boldsymbol{H}$ or $\boldsymbol{E}$ over the entire boundary of the domain of interest. Similarly, (5b) requires that either $\hat{\boldsymbol{n}} \times \boldsymbol{E}$ or $\boldsymbol{H}$ be known on the boundary. However, many problems are fundamentally unbounded in that these quantities can only be specified over the EM source which in general does not completely enclose the region of heterogeneity. The boundary element statements ((13a) and (13b)) provide the necessary relationships between boundary values of $\hat{\boldsymbol{n}} \times \boldsymbol{H}$ and $\boldsymbol{E}$ (or $\hat{\boldsymbol{n}} \times \boldsymbol{E}$ and $\boldsymbol{H}$). In the hyperthermia context, these equations are applied in the homogeneous space, exterior to the patient, but containing the EM source. The boundary of this region also includes infinity, but kernels of the type found in (13a) and (13b) can be shown to vanish there [22]; hence, the only contributions to (13a) and (13b) occur from the boundary of the patient and source. By integrating along a path over the patient surface and detached EM source, unknown patient surface quantities are related to known source quantities which provide the information necessary to close the finite element matrix problem on the patient interior.

In the case where $\boldsymbol{E}$ is known on the detached source, the hybrid element method begins with the finite element formulation which provides $N + m$ equations (for the N nodes comprising the patient interior and the m nodes constituting the patient surface) for each nodal degree of freedom:

$$\begin{bmatrix} A_{11} & A_{12} \\ A_{21} & A_{22} \end{bmatrix} \begin{Bmatrix} E_p \\ E_1 \end{Bmatrix} = \begin{bmatrix} 0 & 0 \\ 0 & B \end{bmatrix} \begin{Bmatrix} 0 \\ F_1 \end{Bmatrix} \tag{16}$$

where B is defined in (7) with length m, E_p are the unknowns on the patient interior, and E_1 and F_1 are the unknown $\boldsymbol{E}$ and $\hat{\boldsymbol{n}} \times \boldsymbol{H}$ on the patient surface. The boundary element method provides $m + n$ equations (for the m nodes on the patient surface and the n nodes on the source) for each nodal degree of freedom:

$$\begin{bmatrix} C_{11} & C_{12} \\ C_{21} & C_{22} \end{bmatrix} \begin{Bmatrix} F_1 \\ F_2 \end{Bmatrix} = \begin{bmatrix} D_{11} & D_{12} \\ D_{21} & D_{22} \end{bmatrix} \begin{Bmatrix} E_1 \\ E_2 \end{Bmatrix} \tag{17}$$

where E_2 represents the known $\boldsymbol{E}$ and F_2 the unknown $\hat{\boldsymbol{n}} \times \boldsymbol{H}$ of the source. Inverting the matrix on the left side of (17) and denoting the partitions for this inverted matrix with a tilde results in

$$\begin{Bmatrix} F_1 \\ F_2 \end{Bmatrix} = \begin{bmatrix} \tilde{C}_{11} & \tilde{C}_{12} \\ \tilde{C}_{21} & \tilde{C}_{22} \end{bmatrix} \begin{bmatrix} D_{11} & D_{12} \\ D_{21} & D_{22} \end{bmatrix} \begin{Bmatrix} E_1 \\ E_2 \end{Bmatrix}. \tag{18}$$

By taking the top m equations of (18), F_1 is eliminated in (16), thus

$$\begin{bmatrix} A_{11} & A_{12} \\ A_{21} & A_{22} - B\left[\tilde{C}_{11} D_{11} + \tilde{C}_{12} D_{21}\right] \end{bmatrix} \begin{Bmatrix} E_p \\ E_1 \end{Bmatrix} = \begin{Bmatrix} 0 \\ B\left[\tilde{C}_{11} D_{12} + \tilde{C}_{12} D_{22}\right] \{E_2\} \end{Bmatrix}. \tag{19}$$

Note that the bottom set of equations in (18) is not explicitly required for solution of (19); however, if F_2 is needed to calculate either the loading on the source or the electric field exterior to the body, F_2 can be computed from the bottom half of (18) once E_1 is known from solution of (19).

When $\hat{\boldsymbol{n}} \times \boldsymbol{H}$ is specified on the source boundary (i.e., F_2 known), the matrix algebra is similar to the above except that the bottom set of equations in (18) is needed.

In this case, (19) becomes

$$\begin{bmatrix} A_{11} & A_{12} & 0 \\ A_{21} & A_{22} - B\left[\tilde{C}_{11}D_{11} + \tilde{C}_{12}D_{21}\right] & -B\left[\tilde{C}_{11}D_{12} + \tilde{C}_{12}D_{22}\right] \\ 0 & \tilde{C}_{21}D_{11} + \tilde{C}_{22}D_{21} & \tilde{C}_{21}D_{12} + \tilde{C}_{22}D_{22} \end{bmatrix} \begin{Bmatrix} E_p \\ E_1 \\ E_2 \end{Bmatrix} = \begin{Bmatrix} 0 \\ 0 \\ F_2 \end{Bmatrix}. \tag{20}$$

An alternate approach, which removes the need for the lower set of equations in (18), is to interchange F_2 and E_2 in (17) such that

$$\begin{bmatrix} C_{11} & -D_{12} \\ C_{21} & -D_{22} \end{bmatrix} \begin{Bmatrix} F_1 \\ E_2 \end{Bmatrix} = \begin{bmatrix} D_{11} & -C_{12} \\ D_{21} & -C_{22} \end{bmatrix} \begin{Bmatrix} E_1 \\ F_2 \end{Bmatrix}. \tag{21}$$

Then, the inversion of the matrix on the left side of (21) can be used to eliminate F_1 in (16):

$$\begin{bmatrix} A_{11} & A_{12} \\ A_{21} & A_{22} - B\left[\tilde{C}_{11}D_{11} - \tilde{D}_{12}D_{21}\right] \end{bmatrix} \begin{Bmatrix} E_p \\ E_1 \end{Bmatrix} = \begin{Bmatrix} 0 \\ B\left[-\tilde{C}_{11}C_{12} + \tilde{D}_{12}C_{22}\right]\{F_2\} \end{Bmatrix} \tag{22}$$

where the tilde notation is again used to represent a partition of the inverse of the left side matrix in (21). Now the bottom set of equations in (21) is not explicitly needed for the solution of (22). If direct solution for the magnetic field is desired, the same procedure with $\hat{\boldsymbol{n}} \times \boldsymbol{E}$ and $\boldsymbol{H}$ playing the roles of $\hat{\boldsymbol{n}} \times \boldsymbol{H}$ and $\boldsymbol{E}$, respectively, can be used.

The left side matrix resulting (in (19) or (22)) from the hybrid coupling has an unusual structure. It is largely sparse owing to the fact that it is largely populated with FEM equations (assuming $E_p > E_1$), but contains a smaller dense region composed of the algebraic BEM equations. For direct solution, the half-bandwidth grows to the number of boundary nodes (for each nodal degree of freedom), which rapidly restricts the size of the problem that can be considered in three dimensions. Further, the bandwidth of the pure FEM equations typically gets quite large in three dimensions, which has encouraged the use of iterative solution techniques in straight three-dimensional finite element applications. (A general rule of thumb for the pure FEM case is that the bandwidth goes as $N^{1/2}$ in two dimensions and $N^{2/3}$ in three dimensions, where N is the total number of nodes in the mesh. Therefore, given a square mesh with ten nodes on a side, the half-bandwidth ≈ 10 in two dimensions but 100 in three dimensions.) In this work we have used well-established direct solution techniques which allowed us to focus on the generation of a consistent set of algebraic equations with a unique solution. However, in order to fully exploit the power of the hybrid approach, careful study of storage and solution schemes for the hybrid algebraic system of equations is needed. In particular, iterative solution techniques such as conjugate gradient methods deserve close attention.

III. Test Cases

In this section the numerical solutions posed in the previous section are compared to analytic solutions for two concentric cylinders of electrically distinct tissues. Three-dimensional test cases have been examined for each of the three numerical approaches—(i) the finite element method (FEM), (ii) the boundary element method (BEM), and (iii) the hybrid element method (HEM)—using two types of boundary conditions specified on the outer cylinder boundary—(i) $\hat{\boldsymbol{n}} \times \boldsymbol{H}$ and (ii) $\boldsymbol{E}$—and a variety of different cylinder radii, tissue electrical properties, and grid discretizations. The results that are shown here are intended to be representative examples of the type of calculations made and the accuracy obtained with fairly coarse grid resolutions (for a more detailed discussion of such results and a derivation of the analytic solutions, see [23]).

Fig. 1(a)–(c) shows FEM, BEM, and HEM results for the magnitude of $\boldsymbol{E}$ versus radius through the midplane of finite length cylinders. The concentric cylinders, which contained electrically distinct media (tissues), were excited at 70 MHz. A known value of $\hat{\boldsymbol{n}} \times \boldsymbol{H}$ was imposed at the boundary of the outer cylinder such that $\boldsymbol{H}$ had magnitude H_0 and direction longitudinally parallel to the cylinder boundary. The worst-case error in these plots is within 4 percent, 2 percent, and 3 percent of the analytic $\boldsymbol{E}$ for the FEM, BEM, and HEM, respectively.

Fig. 2 indicates the numerical discretizations that were used in obtaining the solutions in Fig. 1. For the pure FEM solution, the grid was constructed with $\Delta\varphi = 30°$, $\Delta r = 3.125$ cm, $\Delta z = 10$ cm, resulting in cylinder lengths of 50 cm, an outer radius of 25 cm, and an inner radius of 12.5 cm. Analytic values of $\hat{\boldsymbol{n}} \times \boldsymbol{H}$ were prescribed at the boundary nodes comprising the ends of the cylinder configuration. The BEM mesh used $\Delta\varphi = 30°$ and $\Delta\varphi = 20°$ on the inner and outer cylinders while Δz varied from 12 cm to 16.5 cm. This nodal spacing generated cylinders that were 100 cm in length with inner and outer radii of 15 cm and 25 cm, respectively. As in the FEM case, analytic values could be imposed at the cylinder ends. However, since the midplane solution was of interest, the ends of the cylinders were not discretized (see Fig. 2(b))—the argument being that if the cylinders are long enough relative to the effective radius of the Green function influence, the ends do not effect the midplane solution. Instead, the nodes that would be required to construct the cylinder ends (a sizable number, e.g., see Fig. 2(a)) were used to extend the length of the cylinders and to improve circumferential resolution.

The effects on the numerical solution of leaving the ends off the boundary element cylinders are shown in Fig. 3(a)

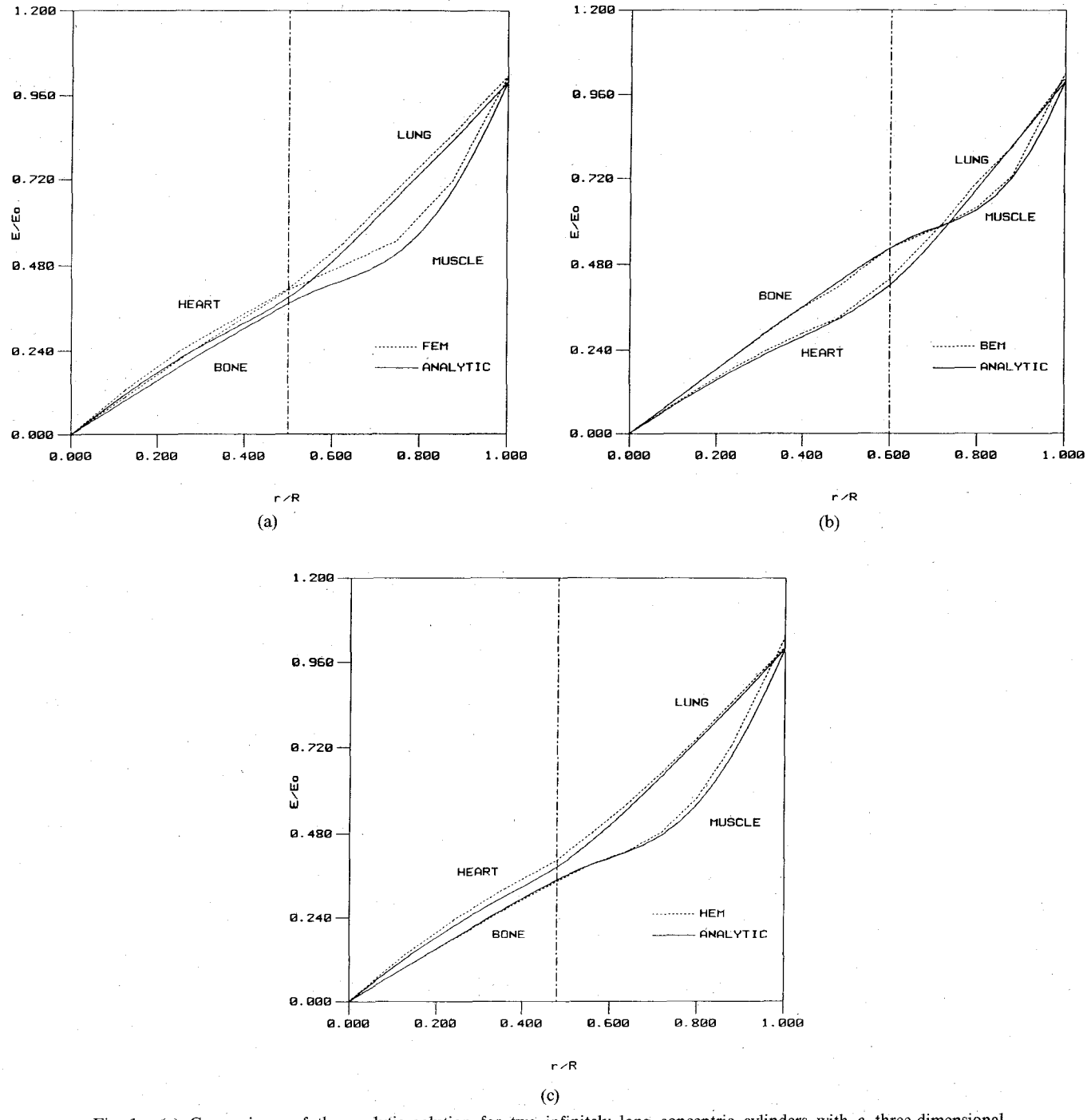

Fig. 1. (a) Comparisons of the analytic solution for two infinitely long concentric cylinders with a three-dimensional numerical solution for two concentric cylinders of finite length. The excitation frequency was 70 MHz and $\hat{n} \times H$ was imposed at $R = 25$ cm. Two different cases are shown: (i) heart ($\epsilon_r = 89$, $\sigma = 0.93\ \Omega^{-1}\mathrm{m}^{-1}$) surrounded by lung ($\epsilon_r = 40$, $\sigma = 0.35\ \Omega^{-1}\mathrm{m}^{-1}$), (ii) bone ($\epsilon_r = 10.5$, $\sigma = 0.02\ \Omega^{-1}\mathrm{m}^{-1}$) surrounded by muscle ($\epsilon_r = 72$, $\sigma = 0.89\ \Omega^{-1}\mathrm{m}^{-1}$). The FEM was used with an inner cylinder radius of 12.5 cm as indicated by the dotted vertical line. (b) Same as (a) except that the BEM was used with an inner cylinder radius of 15 cm. (c) Same as (a) except that the HEM was used with an inner cylinder radius of 12 cm. The inner cylinder was constructed from finite elements while the outer cylinder was composed of boundary elements.

and (b). The BEM solution with E imposed at the radius of a single cylinder with the same dimensions as the outer cylinder in Fig. 2(b), but with discretized ends ($\Delta\varphi = 20°$, $\Delta r = 5$ cm) is displayed in Fig. 3(a). The magnitude of E versus radius for five different cross-sectional planes, which begin at the midplane and move toward the cylinder end, is plotted. For these calculations, the analytic solution was imposed at each cylinder end as in the FEM case. The corresponding calculations are plotted in Fig. 3(b) for the cylinder with the ends removed. The decay in the numerical results (relative to the analytic solution) is apparent as the nondiscretized end of the cylinder is approached. Nonetheless, the numerical calculations near the midplane with or without the cylinder ends discretized are essentially

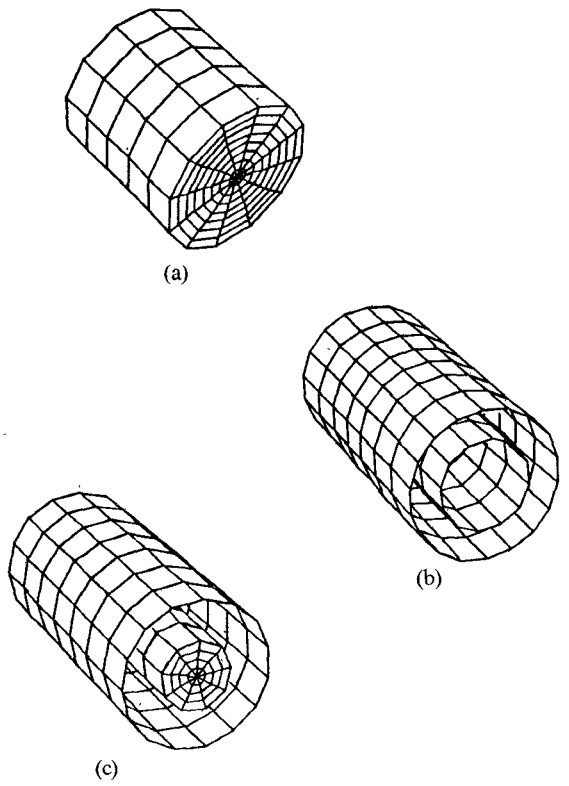

Fig. 2. Three-dimensional test case grids for the (a) finite (FEM), (b) boundary (BEM), and (c) hybrid (HEM) element methods.

indistinguishable and compare quite well to their analytic counterpart, as shown. In general, we do not recommend leaving off the ends of the cylinders (which changes the numerically solved problem); however, by doing so we were able to find a simple test case with which to explore three-dimensional discretization errors on a relatively small computer (MicroVax II).

The HEM solution was achieved with $\Delta\varphi = 40°$, $\Delta r = 3$ cm, and $\Delta z = 15$ cm in the finite element region, and $\Delta\varphi = 24°$, $\Delta z = 15$ cm in the boundary element portion of the mesh which produced cylinders 105 cm in length with inner and outer radii of 12 cm and 25 cm. The same strategy regarding the ends of the cylinders used in the BEM case was taken for the HEM, except at the finite element portion of the grid, where the cylinder ends were discretized and the analytic solution was imposed. To achieve the interaction of all three Cartesian components of $\boldsymbol{E}$, the long axis of the cylinders was tilted 45° off the z axis of the Cartesian coordinate system. Cases have also been examined where the long axis of the cylinders was tilted to various other degrees, and no effect in the magnitude of $\boldsymbol{E}$ was observed [23].

A set of results complementary to those of Fig. 1(a)–(c) should be mentioned. In these computations a known value of $\boldsymbol{E}$ (having magnitude E_0 and direction parallel to the long axis of the cylinders) was imposed at the boundary of the outer cylinder. The cylinder configuration again contained two electrically distinct tissues and was excited at 70 MHz. The same mesh spacings and grid sizes shown in Fig. 2 were used in these calculations as well. Also, as

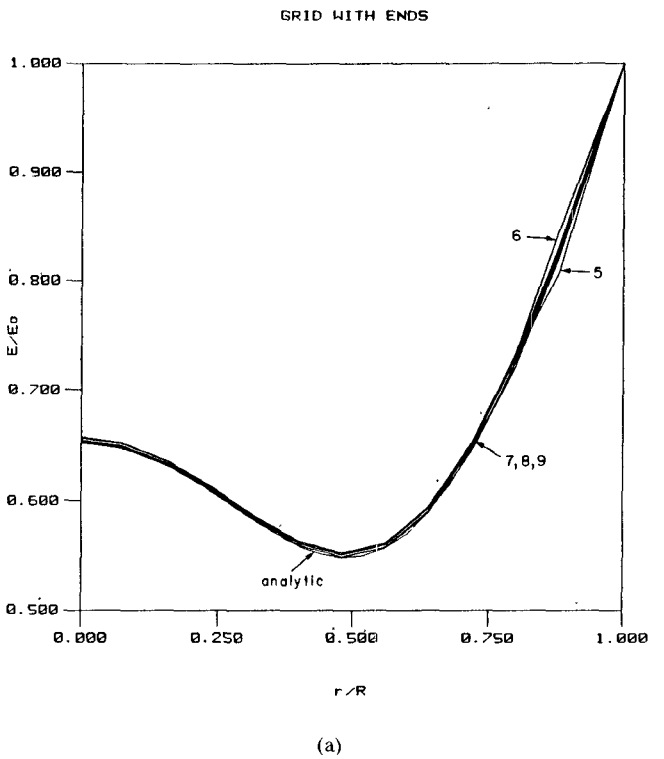

(a)

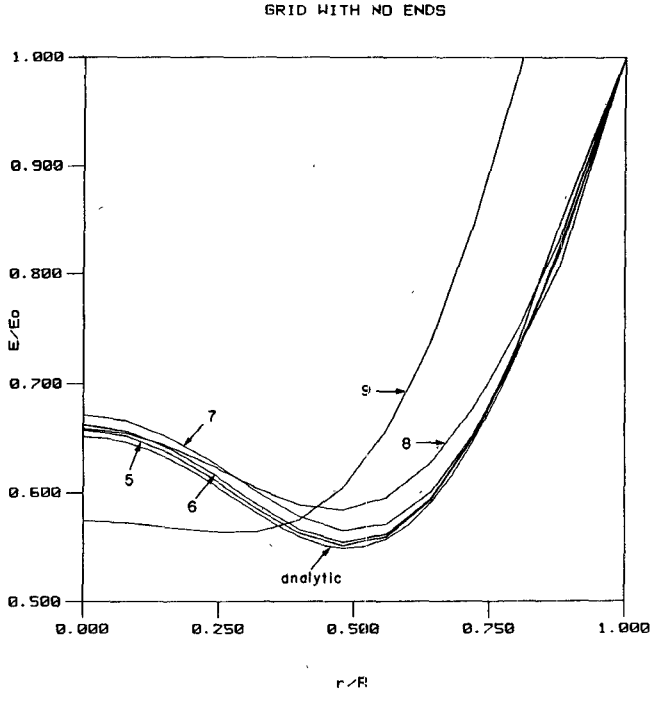

(b)

Fig. 3. (a) Comparison of the analytic solution for a single infinitely long cylinder with the three-dimensional BEM solution for a cylinder of finite length with its ends discretized. The cylinder is lung-filled ($\epsilon_r = 40$, $\sigma = 0.35\ \Omega^{-1}\mathrm{m}^{-1}$), excited at 70 MHz, and has $\boldsymbol{E}$ imposed at $R = 25$ cm. The numbers shown indicate the relative distance from the cylinder midplane where the cylinder length has been normalized to 10 (e.g., 5 denotes the midplane). (b) Same as (a) except that the BEM solution has been computed with the cylinder ends removed. The decay in the numerical solution (relative to the analytic) as the cylinder ends are approached is clear.

described above, the cylinders were rotated 45° off the z axis for full interplay between the components of $\boldsymbol{E}$. The accuracy of the numerical solutions was found to be within 5 percent, 2 percent, and 3 percent of the imposed analytic $\boldsymbol{E}$ for the FEM, BEM, and HEM, respectively [23]. The overall accuracy of all three methods, as shown in Fig. 1(a)–(c), is quite satisfying, especially in view of the coarse computational grids shown in Fig. 2.

IV. Clinical Example

One of the more challenging design problems in clinical hyperthermia is the effective heating of deep-seated tumors. Considerable effort has been devoted to the development of noninvasive regional EM hyperthermia systems, and the ability of these devices to heat substantial portions of deep-seated tumors to therapeutic levels has been of particular interest. One of the earliest devices proposed was a copper sheet which wraps around the body section to be heated [4]. This type of magnetic induction device has received significant attention in the clinical treatment and numerical modeling realms, and both clinical observations as well as one- and two-dimensional numerical models have suggested that the device is not a promising design for deep heating [8], [10], [25]–[27]. In this section we present a three-dimensional model of this type of device to illustrate an application of our numerical formulations. A more complete discussion of the three-dimensional numerical results that we have obtained for this device and several other types of EM hyperthermia systems can be found in [28].

In order to resolve the geometry of a three-dimensional human body while staying within the confines of a moderate-sized computer (MicroVAX II), the boundary element approach was used in this sample simulation. Fig. 4 shows a three-dimensional boundary element grid of the body. This grid was constructed from cross-sectional anatomical drawings found in [29]. The body front faces in the negative y direction as indicated by the right-hand-rule coordinate axes depicted in the lower left portion of each figure. To keep the number of nodes at a minimum while not sacrificing too much geometric detail, the arms and feet were not included. Further, the interior organs were not discretized; that is, this boundary element model of the body was assumed electrically homogeneous. The mesh in Fig. 4 consists of 300 boundary nodes (900 complex unknowns) with typical nodal spacings of 5–8 cm (which in the worst case, for this example, results in approximately 12 nodes per wavelength). Fig. 5 shows a clinical setting with the subject placed inside the single-turn concentric coil ready for simulated treatment of the lower abdomen. A uniform current density is assumed known on the infinitely thin coil; hence, $\hat{\boldsymbol{n}} \times \boldsymbol{H}$ is presumed known on the source, and the matrix equation given in (14) is closed algebraically. The coil is 35 cm in the z direction (with a radius of 25 cm) and is excited at 13 MHz.

In Figs. 6 and 7, contours of $|\boldsymbol{E}|$ on the body surface are shown. In this particular simulation the body consists of

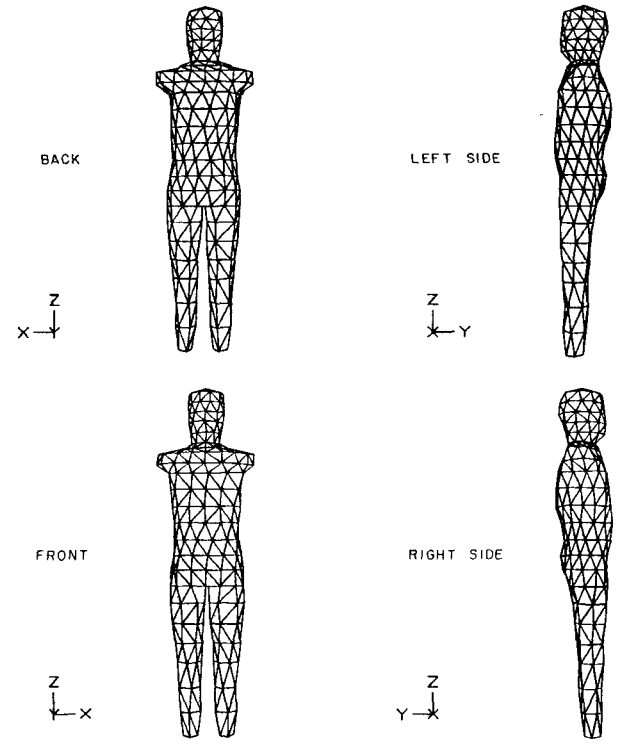

Fig. 4. Three-dimensional boundary element grid of the human body.

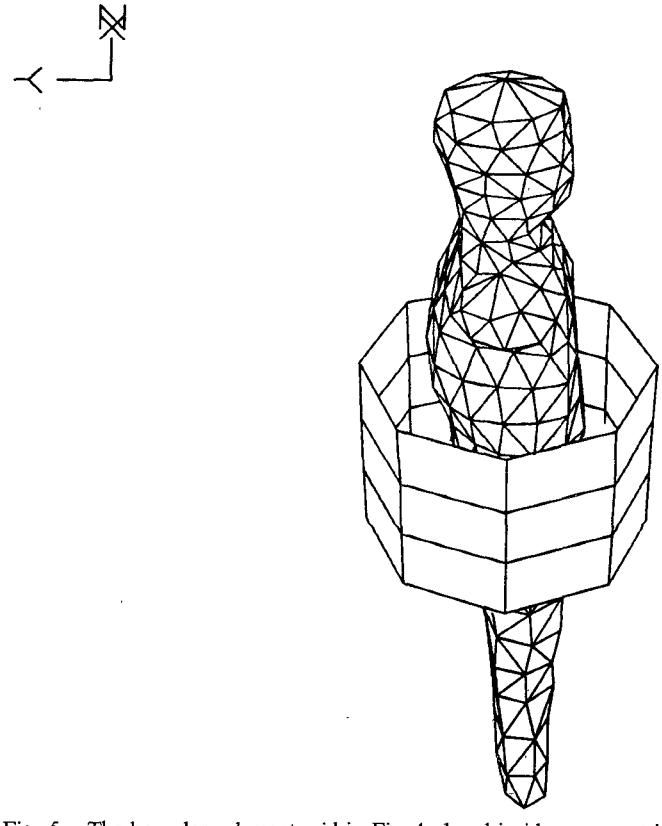

Fig. 5. The boundary element grid in Fig. 4 placed inside a concentric coil positioned for treatment of the lower abdomen.

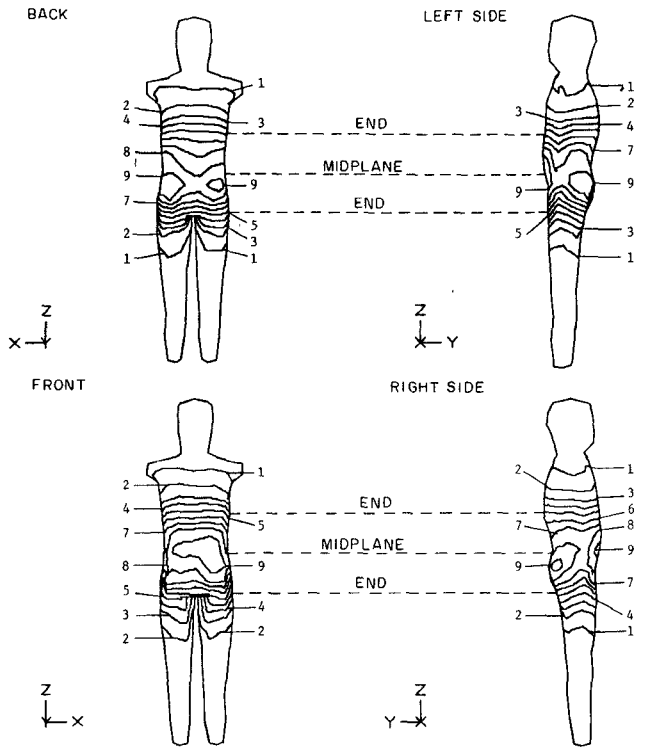

Fig. 6. Contours of $|\boldsymbol{E}|$ produced by the 13 MHz concentric coil model on the exterior surface of the body. The body is muscle-filled ($\epsilon_r = 122$, $\sigma = 0.6\ \Omega^{-1}\mathrm{m}^{-1}$) and the background medium is air. The dotted lines indicate the location of the coil. Contours are scaled to a maximum of 10 and are incremented in steps of unity.

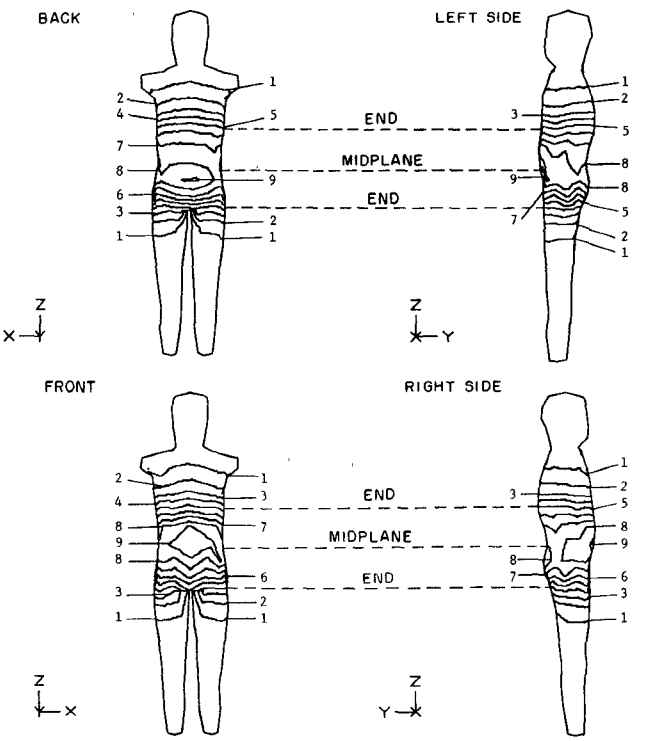

Fig. 7. Same as Fig. 6 for the interior surface of the body. To recover the scale of Fig. 6 multiply by 0.95.

muscle and the background medium is air. Fig. 6 shows $|\boldsymbol{E}|$ contours on the outside body surface (the air side of the air–muscle interface) while Fig. 7 shows the corresponding contours on the inside body surface. The contour lines in these figures are fairly uniform around the body above and below the coil where the body diameter is relatively constant, but show some circumferential variation inside the coil where the body surface is radially less uniform. Figs. 6 and 7 also indicate that the magnitude of the surface electric field is largest on the body portion inside the coil, but falls off rapidly in the z direction, with effectively no fields present above the shoulder region or below the midportion of the thighs. This kind of result is pertinent to hyperthermia treatment planning and equipment design given that other regional EM therapy devices have had problems with heating body portions outside the area of direct exposure [5], [17].

Comparison of Fig. 6 with Fig. 7 shows that the magnitude of the surface electric field is only slightly affected by the air–muscle interface at the body surface. In fact, the scale of Fig. 6 can be recovered in Fig. 7 by multiplying the contour levels in Fig. 7 by 0.95. The degree of similarity between the magnitude distribution on either side of the body surface suggests that the electric field is largely continuous at, and thus, tangential to the body surface throughout the longitudinal dimension. This type of result is also highly relevant to treatment planning and equipment design since some regional devices which produce electric fields that are largely perpendicular to the body surface are believed to create excessive superficial heating due to the electromagnetic jump conditions at such an interface [30].

Contours of $|\boldsymbol{E}|$ in transverse slices through the body have been examined and these results illuminate the weakness of an induction coil for deep-seated hyperthermia. In such cross-sectional slices, the decrease in $|\boldsymbol{E}|$ (to effectively zero) towards the center of the patient was readily apparent regardless of where the transverse section was taken relative to the coil. Large portions of the central axis of the patient had $|\boldsymbol{E}|$ less than 40 percent of the maximum $|\boldsymbol{E}|$ on the body surface. This result occurred throughout the length of the coil with only very small (less than 10 percent of the maximum surface $|\boldsymbol{E}|$) electric fields existing inside the body 10 cm beyond the ends of the coil. These results are discussed more fully in [28].

V. Conclusions

Finite, boundary, and hybrid element formulations for three-dimensional solutions of the Maxwell equations in lossy dielectric media have been presented. These numerical approaches have been implemented as computer algorithms for calculating three-dimensional fields in such heterogeneous media, and have been verified as accurately solving the equations as posed via comparisons with known analytic solutions. Such comparisons have been extensive given that a variety of different tissue electrical properties, geometries, and boundary conditions have been examined. Representative examples have been presented. The basic

problem formulation, while quite general, is of direct interest when simulating hyperthermia treatments for cancer therapy. The usefulness of these algorithms has been shown through a relevant clinical example where the treatment planning and equipment design implications of the results that can be obtained from three-dimensional device simulation have been indicated. These numerical approaches and algorithms should provide a foundation for future simulations of hyperthermia cancer therapy where three-dimensional EM fields need to be calculated in detailed body models.

Studies are beginning to emerge where detailed three-dimensional energy deposition patterns are being calculated inside inhomogeneous three-dimensional models of the body [18], [19]. The competitiveness of the formulations described in this paper with the finite-difference time-domain (FDTD) method has yet to be established for three-dimensional unbounded problems containing a region of high heterogeneity. Certainly, the computational grids used in this work (≈ 300 nodes) are small relative to those achieved in [18] and [19] ($\approx 10^5$ cells). However, while the numerical approaches given herein will always result in a matrix equation (as opposed to the FDTD, where matrices are avoided through explicit time-stepping), iterative solution schemes should significantly reduce the storage requirements of the FEM equations, thereby allowing for greater grid resolutions. Further, these techniques should require considerably fewer unknowns than the FDTD for two reasons: (1) no discretization is needed in the background medium containing the source and heterogeneous object, and (2) the inherent flexibility of finite and boundary elements is such that irregular grid spacing can readily be accommodated, which makes possible efficient meshing of irregular geometries, regions of little or great interest, and regions of large or small field gradients. Thus, further work will be required to quantify the advantages and disadvantages of the methods described herein compared to those of FDTD and other numerical approaches.

REFERENCES

[1] J. W. Strohbehn, "Summary of physical and technical studies," in *Hyperthermic Oncology*, vol. 2, J. Overgaard, Ed. London: Taylor and Francis, 1984.

[2] J. W. Strohbehn and R. B. Roemer, "A survey of computer simulations of hyperthermia treatments," *IEEE Trans. Biomed. Eng.*, vol. BME-31, pp. 136–149, 1984.

[3] H. Kato, M. Hiraoka, T. Nakajima, and T. Ishida, "Deep-heating characteristics of an RF capacitance heating device," *Int J. Hyperthermia*, vol. 1, pp. 15–28, 1985.

[4] F. K. Storm, R. S. Elliott, W. H. Harrison, and D. L. Morton, "Clinical RF hyperthermia by magnetic-loop induction: A new approach to human cancer therapy," *IEEE Trans. Microwave Theory Tech.*, vol. MTT-30, pp. 1149–1158, 1982.

[5] P. F. Turner, "Regional hyperthermia with an annular phased array," *IEEE Trans. Biomed. Eng.*, vol. BME-31, pp. 106–114, 1984.

[6] D. R. Lynch, K. D. Paulsen, and J. W. Strohbehn, "Finite element solution of Maxwell's equations for hyperthermia treatment planning," *J. Comput. Phys.*, vol. 58, pp. 246–269, 1985.

[7] D. R. Lynch, K. D. Paulsen, and J. W. Strohbehn, "Hybrid element method for unbounded electromagnetic problems in hyperthermia," *Int. J. Num. Meth. Eng.*, vol. 23, pp. 1915–1937, 1986.

[8] K. D. Paulsen, J. W. Strohbehn, and D. R. Lynch, "Comparative theoretical performance for two types of regional hyperthermia systems," *Int. J. Radiat. Oncol. Biol. Phys.*, vol. 11, pp. 1659–1671, 1985.

[9] K. D. Paulsen, D. R. Lynch, and J. W. Strohbehn, "Numerical treatment of boundary conditions at points connecting more than two electrically distinct regions," *Commun. Appl Numer. Meth.*, vol. 3, 53–62, 1987.

[10] J. W. Strohbehn, K. D. Paulsen, and D. R. Lynch, "Use of finite element methods in computerized thermal dosimetry," in *Physical Techniques in Clinical Hyperthermia*, J. W. Hand and J. R. James, Eds. Chichester, England: Research Studies Press, 1986.

[11] O. P. Gandhi, J. F. DeFord, and H. Kanai, "Impedance method for calculation of power deposition patterns in magnetically induced hyperthermia," *IEEE Trans. Biomed. Eng.*, vol. BME-31, pp. 644–651, 1984.

[12] M. F. Iskander, P. F. Turner, J. B. DuBow, and J. Kao, "Two-dimensional technique to calculate the EM power deposition pattern in the human body," *J. Microwave Power*, vol. 17, pp. 175–185, 1982.

[13] P. M. Van Den Berg, A. T. De Hoop, A. Segal, and N. Praagman, "A computational model of electromagnetic heating of biological tissue with application to hyperthermic cancer therapy," *IEEE Trans. Biomed. Eng.*, vol. BME-30, pp. 797–805, 1983.

[14] K. M. Chen, "Interaction of electromagnetic fields with biological bodies," in *Research Topics in Electromagnetic Theory*, J. A. Kong, Ed. New York: Wiley, 1980.

[15] M. J. Hagmann, O. P. Gandhi, and C. H. Durney, "Numerical calculations of electromagnetic energy deposition for a realistic model of man," *IEEE Trans. Microwave Theory Tech.*, vol. MTT-27, pp. 804–809, 1979.

[16] M. K. Hessary and K. M. Chen, "EM local heating with HF electric fields," *IEEE Trans. Microwave Theory Tech.*, vol. MTT-32, pp. 569–576, 1984.

[17] M. J. Hagmann and R. L. Levin, "Aberrant heating: A problem in regional hyperthermia," *IEEE Trans. Biomed. Eng.*, vol. BME-33, pp. 405–411, 1986.

[18] D. M. Sullivan, D. T. Borup, and O. P. Gandhi, "Use of the finite-difference time-domain method in calculating EM absorption in human tissues," *IEEE Trans. Biomed. Eng.*, vol. BME-34, pp. 148–157, 1987.

[19] D. M. Sullivan, O. P. Gandhi, and A. Taflove, "Use of the finite-difference time domain method in calculating EM absorption in man models," submitted to *IEEE Trans. Biomed. Eng.*

[20] W. G. Gray, "On normal flow boundary conditions in finite element codes for two-dimensional shallow water flow," *Int. J. Numer. Meth. Fluids*, vol. 4, pp. 99–104, 1984.

[21] M. S. Engleman, R. L. Sani, and P. M. Gresho, "The implementation of normal and/or tangential boundary conditions in finite element codes for incompressible fluid flow," *Int J. Numer. Meth. Fluids*, vol. 2, pp. 225–238, 1982.

[22] J. A. Stratton, *Electromagnetic Theory* London: McGraw-Hill, 1941.

[23] K. D. Paulsen, "Finite, boundary, and hybrid element solution of the Maxwell equations for simulating hyperthermia treatment of cancer," Ph.D. thesis, Dartmouth College, Hanover, NH, 1986.

[24] F. A. Gibbs, "Regional hyperthermia: A clinical appraisal of noninvasive deep-heating methods," *Cancer Res.* (suppl.), vol. 44, pp. 4765s–4770s, 1984.

[25] S. Halac, R. B. Roemer, J. R. Oleson, and T. C. Cetas, "Magnetic induction heating of tissue: Numerical evaluation of tumor temperature distributions," *Int. J. Radiat. Oncol. Biol. Phys.*, vol. 9, pp. 881–891, 1983.

[26] J. R. Oleson, R. S. Heusinkveld, and M. R. Manning, "Hyperthermia by magnetic induction: II. Clinical experience with concentric electrodes," *Int. J. Radiat. Oncol. Biol. Phys.*, vol. 9, pp. 549–556, 1983.

[27] J. W. Strohbehn, "Theoretical temperature distributions for solenoidal-type hyperthermia systems," *Med. Phys.*, vol. 9, pp. 673–682, 1982.

[28] K. D. Paulsen, J. W. Strohbehn, and D. R. Lynch, "Theoretical electric field distributions produced by three types of regional hyperthermia devices in a three-dimensional homogeneous model of man, *IEEE Trans. Biomed. Eng.*, vol 35, pp. 36–45, 1988.

[29] A. C. Eycleshynmer and D. M. Schoemaker, "*A Cross-Section Anatomy*. New York: Appleton, Century, and Crofts, 1970.

[30] R. S. Elliott, W. A. Harrison, and F. K. Storm, "Hyperthermia: Electromagnetic heating of deep-seated tumors," *IEEE Trans. Biomed. Eng.*, vol. BME-29, pp. 61–64, 1982.

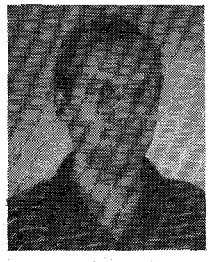

Keith D. Paulsen (S'85–M'86) received the B.S. in biomedical engineering from Duke University, Durham, NC, in 1981 and the M.S. and Ph.D. degrees in engineering from Dartmouth College, Hanover, NH, in 1984 and 1986, respectively.

He is currently an Assistant Professor in the Department of Electrical and Computer Engineering at the University of Arizona, Tucson, AZ. His research interests include numerical electromagnetics with application to biomedical problems.

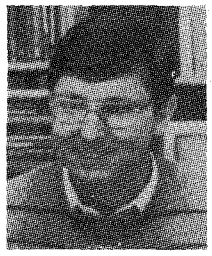

Daniel R. Lynch was born in Glens Falls, NY, on January 10, 1950. He received the B.S. and M.S. degrees in mechanical engineering from the Massachusetts Institute of Technology, Cambridge, in 1972 and the M.S. and Ph.D. degrees in civil engineering from Princeton University, Princeton, NJ, in 1976 and 1978, respectively.

He has worked as a power engineer and a biomedical engineer and is currently Associate Professor at Dartmouth College's Thayer School of Engineering, where he has taught since 1978.

John W. Strohbehn (S'57–M'64–SM'81), for a photograph and a biography, please see the May 1986 issue of this TRANSACTIONS.